

SN 2024abfl: A Low-Luminosity Type IIP Supernova in NGC 2146 from a Low-Mass Red Supergiant Progenitor

Xiaohan Chen^{1,2}, Ning-Chen Sun^{3,1,4,★}, Qiang Xi^{3,1}, Chun Chen^{5,6,7}, Yu Zhang¹, Zexi Niu^{3,1}, Junjie Jin¹, Yiming Mao^{1,3}, Beichuan Wang^{1,3}, Samaporn Tinyanont⁸, Krittidas Chanchaiworawit⁸, Kanthanakorn Noysena⁸, David Aguado^{9,10}, Ismael Perez-Fournon^{9,10}, Frédéric Poidevin^{9,10}, Justyn R. Maund¹³, Xunhao Chen^{1,3}, Pengliang Du¹, David López Fernández-Nespral^{9,10}, Liguo Fang¹, Guolin Gao^{1,2}, Jiupeng Guo¹, Min He¹, Xinyi Hong^{1,3}, Zhigang Hou¹, Qingzheng Li¹, Wenxiong Li¹, Tongyu Liu¹, Alicia López-Oramas^{9,10}, Haiyang Mu¹, César Rojas-Bravo^{3,1}, Jianfeng Tian¹, Jinhua Wang¹, Lingzhi Wang^{15,16}, Rui Wang¹, Yanan Wang¹, Ziyang Wang^{11,12}, Klaas Wiersema¹⁴, Ying Wu¹, Guo Zhen^{17,18}, Jie Zheng¹, Guoyin Zhu¹, Yinan Zhu¹, Zhou Fan^{1,3,★★}, Jing Li^{2,★★★}, Hong Wu^{1,3}, and Jifeng Liu^{1,3,4}

¹ National Astronomical Observatories, Chinese Academy of Sciences, Beijing 100101, China

² School of Physics and Astronomy, China West Normal University, Nanchong 637002, China

³ School of Astronomy and Space Science, University of Chinese Academy of Sciences, Beijing 100049, China

⁴ Institute for Frontiers in Astronomy and Astrophysics, Beijing Normal University, Beijing, 102206, China

⁵ School of Physics and Astronomy, Sun Yat-sen University, Zhuhai 519082, China

⁶ CSST Science Center for the Guangdong-Hong Kong-Macau Greater Bay Area, Sun Yat-sen University, Zhuhai 519082, China

⁷ Dipartimento di Fisica, Università di Napoli “Federico II”, Compl. Univ. di Monte S. Angelo, Via Cinthia, I-80126, Napoli, Italy

⁸ National Astronomical Research Institute of Thailand, 260 Moo 4, Donkaew, Maerim, Chiang Mai, 50180, Thailand

⁹ Instituto de Astrofísica de Canarias, Vía Láctea, 38205 La Laguna, Tenerife, Spain

¹⁰ Universidad de La Laguna, Departamento de Astrofísica, 38206 La Laguna, Tenerife, Spain

¹¹ School of Physics and Astronomy, Beijing Normal University, Beijing 100875, China

¹² Department of Physics, Faculty of Arts and Sciences, Beijing Normal University, Zhuhai 519087, China

¹³ Department of Physics, Royal Holloway, University of London, Egham, TW20 0EX, United Kingdom

¹⁴ Centre for Astrophysics Research, University of Hertfordshire, Hatfield, AL10 9AB, UK

¹⁵ Chinese Academy of Sciences South America Center for Astronomy (CASSACA), National Astronomical Observatories, CAS, Beijing 100101, China

¹⁶ Departamento de Astronomía, Universidad de Chile, Las Condes, 7591245 Santiago, Chile

¹⁷ Instituto de Física y Astronomía, Universidad de Valparaíso, ave. Gran Bretaña, 1111, Casilla 5030, Valparaíso, Chile

¹⁸ Millennium Institute of Astrophysics, Nuncio Monseñor Sotero Sanz 100, Of. 104, Providencia, Santiago, Chile

Received September 30, 20XX

ABSTRACT

Type IIP supernovae (SNe IIP) exhibit a significant diversity in their explosion properties, yet the physical mechanisms driving this diversity remain unknown. In this work, we present photometric and spectroscopic observations of SN 2024abfl, a SN IIP in NGC 2146 with a directly detected red supergiant (RSG) progenitor. We find it has a low plateau luminosity ($M_V \sim -15$ mag) and a relatively long plateau length (~ 126.5 days). By fitting a semi-analytical model, we estimated a ^{56}Ni mass of $\sim 0.009 M_\odot$, an initial kinetic energy of ~ 0.42 foe, an initial thermal energy of ~ 0.03 foe and an ejecta mass of $\sim 8.3 M_\odot$. The spectral evolution of SN 2024abfl is similar to those of other SNe IIP, except for much lower ejecta velocities at similar epochs. At later epochs, we find a relatively high-velocity H α absorption feature at $\sim -4000 \text{ km s}^{-1}$, possibly due to a fast-moving plume of matter in the inner ejecta, and two emission features at $\pm 2000 \text{ km s}^{-1}$, possibly caused by CSM interaction. We estimate the progenitor mass to be $\leq 15 M_\odot$ based on nebular spectra. We conclude that SN 2024abfl is a low-luminosity SN IIP originating from a low-mass RSG progenitor.

Key words. supernovae – core-collapse supernovae – stellar evolution

1. Introduction

Massive stars ($\gtrsim 8 M_\odot$) burn hydrogen into helium during the main-sequence phase, followed by helium burning that produces a carbon-oxygen core. As the core continues to contract and heat up, carbon and oxygen are ignited, triggering a series of

further nuclear reactions that ultimately form an iron core. The core then collapses, leading to a core-collapse supernovae (CCSNe). Type IIP supernovae (SNe IIP, hereafter) are a subclass of hydrogen-rich CCSNe and are characterized by a pronounced plateau in their light curves lasting ~ 100 days (Filippenko 1997; Arcavi 2017). After core collapse, the outer envelope is ejected, heated, and ionized by the shock wave. As the ejecta expand, the recombination front moves inward in mass coordinates, causing the radius and temperature of the photosphere to remain

* Email: sunnc@ucas.ac.cn

** Email: zfan@nao.cas.cn

*** Email: lijing@bao.ac.cn

nearly constant. This results in energy being released at an approximately constant rate, thereby producing the plateau in the light curve of SNe IIP. When the recombination front approaches the inner boundary of the hydrogen envelope and the entire hydrogen envelope has recombined, the luminosity drops abruptly (Alsabti & Murdin 2017).

They are widely believed to originate from the explosions of red supergiants (RSGs)—stars with very massive hydrogen envelopes (Grassberg et al. 1971; Chevalier 1976; Falk & Arnett 1977; Arnett 1980). Direct imaging has confirmed that RSGs are the progenitor stars of SNe IIP (e.g. Van Dyk et al. 2003; Fraser 2016; Niu et al. 2023). However, a persistent discrepancy exists between the RSG mass range predicted by stellar evolution models and that inferred from direct detections of SNe IIP progenitors. This inconsistency is commonly termed the "RSG problem" (Smartt 2009). Specifically, modern stellar evolution models (Heger et al. 2003; Eldridge & Tout 2004) indicate that stars with initial masses of approximately 8–25 M_{\odot} should evolve into RSGs after completing nuclear burning and ultimately explode as CCSNe. However, in the direct detections of progenitors, no RSGs with initial masses $> 18 M_{\odot}$ have been directly linked to observed Type IIP SNe. Most confirmed progenitors fall within a lower mass range (concentrated around 8–16 M_{\odot}), suggesting that higher-mass RSG progenitors appear to be "missing." Currently, there are primarily four explanations. One possible explanation is that this may result from the currently small sample size of detected SNe IIP progenitors, leading to finite sample effects (Davies & Beasor 2018). Additionally, some studies point out that the progenitor mass may be mismeasured due to uncertainties in photometric measurements such as stellar pulsation and circumstellar extinction (Niu et al. 2023; Hong et al. 2024) or due to the blending of unresolved field stars (Zhao et al. 2025). Alternatively, the so-called failed supernova hypothesis proposes that a significant fraction of massive RSGs may not undergo successful explosions. Instead, they collapse directly into black holes, with only a small fraction of the stellar envelope being ejected (Nadezhin 1980; Lovegrove & Woosley 2013; Kochanek 2014). A further explanation is that massive RSGs may undergo significant structural changes at certain evolutionary phases, thereby deviating from their initially predicted evolutionary paths (de Jager 1998; Ekström et al. 2012; Georgy 2012; Suzuki & Shigeyama 2025).

Some detailed studies of the SNe IIP population have been conducted with comprehensive observations and modeling (Hamuy 2003; Das et al. 2025b). These studies show that they cover a wide range of plateau luminosities ($-18 < M_V < -13$), ^{56}Ni mass ($0.001\text{--}0.26 M_{\odot}$), explosion energies (0.1–5.5 foe) and ejecta masses ($5.4\text{--}24.8 M_{\odot}$). Some SNe IIP constitute a low-luminosity subclass (LLSNe IIP; Das et al. 2025a). These events are characterized by narrow spectral lines (indicative of low expansion velocities), faint magnitudes ($M_{r,\text{peak}} \geq -16$), low ^{56}Ni mass ($0.001\text{--}0.025 M_{\odot}$) and low explosion energies (0.1–0.28 foe) (Pastorello et al. 2004; Das et al. 2025b). Studies have found that LLSNe IIP mostly originate from low-mass RSG progenitor stars ($8\text{--}12 M_{\odot}$). It is worth noting, however, stars of this mass range account for ~ 50 per cent of all massive stars, but only approximately 19 per cent of SNe IIP explode as LLSNe IIP (Das et al. 2025a). This indicates a significant diversity in the explosion of low-mass RSG supergiants, but the physical mechanisms remains unknown. Therefore, more detailed studies of LLSNe IIP are still needed.

SN 2024abfl is a SN IIP discovered by Koichi Itagaki (Teppo-cho, Yamagata, Japan) on 2024 November 15.5840 UT (MJD = 60629.58) in the galaxy NGC 2146 at an apparent mag-

nitude of 17.5 in the clear band (Itagaki 2024), as shown in Figure 1. The redshift of the host galaxy is $z = 0.002979$, as reported by the Transient Name Server (TNS). Soon after discovery, Luo et al. (2025) reported the direct detection of a RSG progenitor in pre-explosion images from the Hubble Space Telescope. Their analysis indicated an initial mass of $9\text{--}12 M_{\odot}$. Gerard et al. (2026) conducted a detailed analysis of SN 2024abfl and classified it as a LLSNe. Therefore, SN 2024abfl is an important target for studying LLSNe IIP.

In this paper, we present observations of SN 2024abfl and a detailed analysis of its light curve and spectral evolution. This paper is organized as follows. In Section 2, we describe our observations of SN 2024abfl. Section 3 discusses the host galaxy of SN 2024abfl. Section 4 presents the photometric analysis, while Section 5 describes the spectroscopic analysis. In Section 6, we summarize our conclusions.

2. Observations

2.1. Photometry

We conducted a multi-band photometric monitoring campaign of SN 2024abfl with the Xinglong 60-cm telescope (XL-60), the Xinglong 35-cm telescope (XL-35), the Thai Robotic Telescope (TRT) network and the Liverpool Telescope (LT). The observations cover the g , r , i , and B , V , R , I bands. We triggered the follow-up observations from $t = 4.4$ days to $t = 379.0$ days. All the images were processed using standard reduction procedures, including bias subtraction and flat-field correction. Point-spread-function (PSF) photometry was then performed with the Automated Photometry of Transients (AUTOPHOT) package (Brennan & Fraser 2022). Since SN 2024abfl is located in the outskirts of its host galaxy, where the host contribution is negligible, we perform direct photometry without image subtraction.

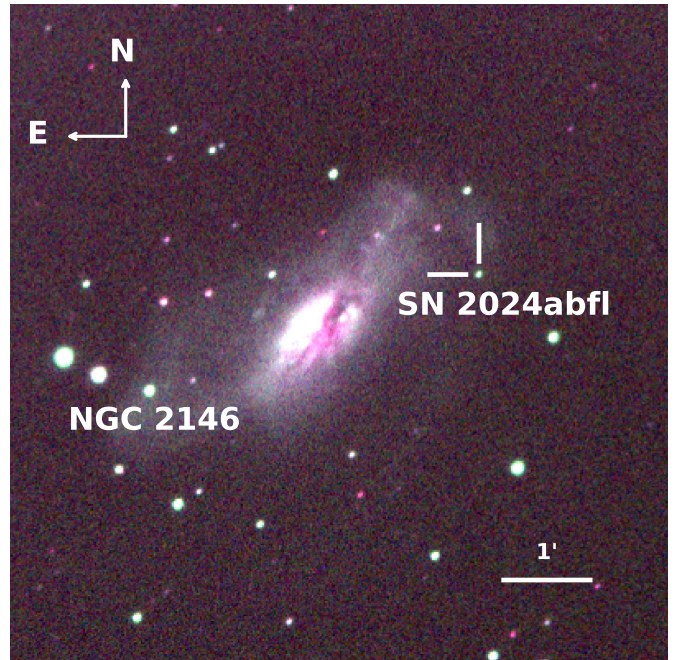


Fig. 1: SN 2024abfl and its host galaxy NGC 2146. Shown is an RGB composite assembled from Xinglong 35-cm telescope g -, r -, and i -band exposures at $t = 4.4$ days after the explosion.

Table 1: Ultraviolet-optical photometric results of SN 2024abfl. We only show the first 15 rows; the full table is available online. Magnitudes are reported in the default photometric systems: Johnson-Cousins *BVRI* and Swift/UVOT bands are calibrated in the Vega system, whereas SDSS *gri* and ATLAS *c* and *o* bands are calibrated in the AB system. The phase represents days relative to the date of explosion, $t_0 = 60627.27$ MJD.

MJD	Phase	Filter	Magnitude	Uncertainty	Instrument
60628.2	1.0	<i>g</i>	17.26	0.22	ZTF
60628.3	1.0	<i>r</i>	17.44	0.03	ZTF
60629.6	2.3	<i>o</i>	17.17	0.05	ATLAS
60631.3	4.0	<i>r</i>	17.20	0.10	ZTF
60631.5	4.2	<i>o</i>	16.98	0.03	ATLAS
60631.7	4.4	<i>i</i>	17.03	0.06	XL-35
60631.7	4.4	<i>g</i>	16.99	0.04	XL-35
60633.0	5.7	<i>B</i>	17.37	0.30	XL-60
60633.7	6.4	<i>i</i>	16.82	0.08	XL-35
60633.7	6.4	<i>g</i>	17.11	0.06	XL-35
60634.0	6.7	<i>B</i>	16.94	0.23	XL-60
60634.0	6.7	<i>V</i>	16.69	0.19	XL-60
60634.0	6.7	<i>R</i>	16.6	0.12	XL-60
60634.0	6.7	<i>I</i>	16.41	0.14	XL-60
60634.7	7.4	<i>i</i>	17.23	0.07	XL-35

The galaxy NGC 2146 also hosted SN 2018zd, a previous event proposed to have an electron-capture origin (Hiramatsu et al. 2021). Swift’s long-term monitoring campaign of SN 2018zd serendipitously covered the first few days after the explosion of SN 2024abfl. We retrieved the corresponding UVOT data obtained with the *UVW2*, *UVM2*, and *UVW1* filters¹. Aperture photometry was performed with HEASoft/uvotsource, adopting a 3" extraction radius. Flux subtraction of the host background was applied based on the pre-explosion images.

We also obtained ATLAS and ZTF data for SN 2024abfl using their forced-photometry services (Tonry et al. 2018; Masci et al. 2018). All photometric results are listed in Table 1.

2.2. Spectroscopy

Spectroscopic monitoring of SN 2024abfl was conducted from $t = 3.6$ days to $t = 198.6$ days with two facilities: the Xinglong 2.16-m telescope (XL-216) and 2.56-m Nordic Optical Telescope (NOT). The spectral reduction was performed with standard IRAF routines, involving bias subtraction, flat-field correction, cosmic-ray removal, flux calibration and wavelength calibration.

Additionally, two publicly available spectra were retrieved from TNS: one obtained with the Frederick C. Gillett Gemini North Telescope (Gemini-N) at $t = 3.2$ days, and the other with the 2.01-m Himalayan Chandra Telescope (HCT) at $t = 2.6$ days (Das et al. 2024; Andrews et al. 2024). A log of all spectroscopic observations is listed in Table 2.

3. Host Galaxy

SN 2024abfl is located in the outskirts of NGC 2146, a nearby starburst galaxy that has undergone a recent merger event (Adamo et al. 2012a). In this section, we discuss the distance, metallicity, and extinction of the host galaxy, which are essential for the analysis of SN 2024abfl.

3.1. Distance

The NASA/IPAC Extragalactic Database (NED) lists 16 distance measurements for NGC 2146, of which 13 are based on the Tully-Fisher method (Bottinelli et al. 1983), one on the Sosies method (Terry et al. 2002), and the remaining two on the tip of the red giant branch (TRGB) method and globular-cluster radius (GC radius) technique (Adamo et al. 2012b), respectively. Distances derived with the Tully-Fisher method span 10.3–39.7 Mpc, the Sosies approach gives 27.7 Mpc, and both the TRGB and GC radius techniques yield 18 Mpc. Because NGC 2146 underwent a strong tidal interaction with another galaxy within the last Gyr, the scatter of the Tully-Fisher relation becomes significantly larger for such an interacting system (Callis et al. 2021). For NGC 2146, we adopt the $15.6^{+6.1}_{-3.0}$ Mpc distance provided by the combined probability distribution of kinematic, Tully-Fisher and GC-radius measurements (Callis et al. 2021).

3.2. Metallicity

De Vis et al. (2019) used literature and VLT/MUSE emission line fluxes to derive gas-phase metallicities (oxygen abundances) for more than 10,000 individual regions, and they also determined characteristic metallicities for each galaxy. For NGC 2146, they reported a global gas-phase metallicity of $12 + \log(\text{O/H}) = 8.78 \pm 0.16$ ², equal to $1.2 Z_{\odot}$. SN 2024abfl is situated in the outskirts of NGC 2146 (as shown in Figure 1), where the metallicity is expected to be lower.

3.3. Extinction

To obtain a more accurate understanding of SN 2024abfl, it is essential to estimate the total line-of-sight extinction toward it. The Galactic extinction toward NGC 2146 is $A_V^{\text{MW}} = 0.26$ mag according to Schlafly & Finkbeiner (2011). For host extinction, there are two commonly used methods for a rough estimation: (i) the equivalent width (EW) of the Na I D absorption line, (ii) the $(V - I)$ colours.

First, we used the Gemini-N spectrum obtained at $t = 0.9$ days to estimate the host-galaxy extinction by measuring the EW of the Na I D absorption. As shown in Figure 2, two absorption components are present: one near the rest wavelengths of the doublet and another at a higher redshift of $z = 0.0033$. We attribute the former component to the Milky Way and the latter to NGC 2146. Since the Na I D doublet is superimposed with a broad He I emission, the baseline was modeled using a fourth-order polynomial and each absorption feature was fitted with a Gaussian profile. The total EW of the host-galaxy Na I D doublet is $\text{EW}^{\text{Host}} = 0.5 \text{ \AA} + 0.52 \text{ \AA} = 1.02 \text{ \AA}$. The empirical relation between the EW of Na I D and the colour excess $E(B - V)$ derived by Poznanski et al. (2012) is employed to calculate the the colour excess $E(B - V)$. For simplicity, we assume the standard extinction law with $R_V = 3.1$ (Cardelli et al. 1989). This yields a host extinction of $A_V^{\text{Host}} = 0.68 \pm 0.12$ mag.

¹ <https://www.swift.ac.uk/archive/selectseq.php?tid=00010392&spu/1&ships&distance=10.180z1&ne=1&ci=1&ne=1&sorter=portal>

Table 2: Spectroscopic observation of SN 2024abfl. The phase represents days relative to the date of explosion, $t_0 = 60627.27$ MJD.

MJD	Phase (d)	Filter and Grism	Spectral range (Å)	Telescope/Instrument
60629.9	2.6	676R+420 gr/mm	3500-8950	HCT/HFOSC
60630.5	3.2	B480+G5309	3750-7500	Gemini-N/GMOS
60630.9	3.6	385LP+G4	3700-8800	XL-216/BFOSC
60631.9	4.6	385LP+G4	3700-8800	XL-216/BFOSC
60658.6	31.4	385LP+G4	3700-8800	XL-216/BFOSC
60661.7	34.5	385LP+G4	3700-8800	XL-216/BFOSC
60666.9	39.6	385LP+G4	3700-8800	XL-216/BFOSC
60667.9	40.6	385LP+G4	3700-8800	XL-216/BFOSC
60675.6	48.3	385LP+G4	3700-8800	XL-216/BFOSC
60678.8	51.5	385LP+G4	3700-8800	XL-216/BFOSC
60680.7	53.4	385LP+G4	3700-8800	XL-216/BFOSC
60690.7	63.5	385LP+G4	3700-8800	XL-216/BFOSC
60714.6	87.3	385LP+G4	3700-8800	XL-216/BFOSC
60719.5	92.2	385LP+G4	3700-8800	XL-216/BFOSC
60722.5	95.3	385LP+G4	3700-8800	XL-216/BFOSC
60746.6	119.3	385LP+G4	3700-8800	XL-216/BFOSC
60767.5	140.3	385LP+G4	3700-8800	XL-216/BFOSC
60816.9	189.6	Grism #4	3200-9600	NOT/ALFOSC
60825.9	198.6	Grism #4	3200-9600	NOT/ALFOSC

We also use the ‘colour method’ to estimate the host extinction (Olivares E. et al. 2010). This method assumes that all SNe IIP have the same photospheric temperature at the end of the plateau phase ($t_{\text{PT}} - 30$ days), and that color differences are primarily due to host galaxy dust extinction. The calculation formula is as follows:

$$A_V(V-I) = 2.518 [(V-I) - 0.656], \quad (1)$$

$$\sigma(A_V) = 2.518 \sqrt{\sigma_{(V-I)}^2 + 0.0053^2 + 0.0059^2}. \quad (2)$$

We estimated the $(V-I)$ colours (corrected for Galactic extinction) at the end of the plateau phase (~ 100 days) and obtained a result of $A_V^{\text{Host}} = 0.77 \pm 0.51$, which is consistent with the value obtained using the first method within uncertainties.

Ultimately, we adopt the $A_V^{\text{Host}} = 0.68 \pm 0.12$ mag throughout the paper. We note that, however, the result of Gerard et al. (2026) ($E(B-V)_{\text{host}} = 0.01 \pm 0.08$ mag) is lower than ours.

4. Photometric Analysis

4.1. Main light-curve features

The multi-band light curve of SN 2024abfl is shown in Figure 3. The last non-detection of SN 2024abfl in the ZTF_r band was on $t = -0.96$ day, followed by a clear detection on $t = 0.97$ day in the ZTF_g band. We assume the explosion time of SN 2024abfl to be the median of these two epochs, i.e. $t = 0.0 \pm 0.97$ day. Shortly afterward, Koichi Itagaki reported it at MJD = 60629.58 ($t = 2.31$ days). Unless otherwise noted, all epochs in this paper are given relative to the explosion date. In the first few days, the

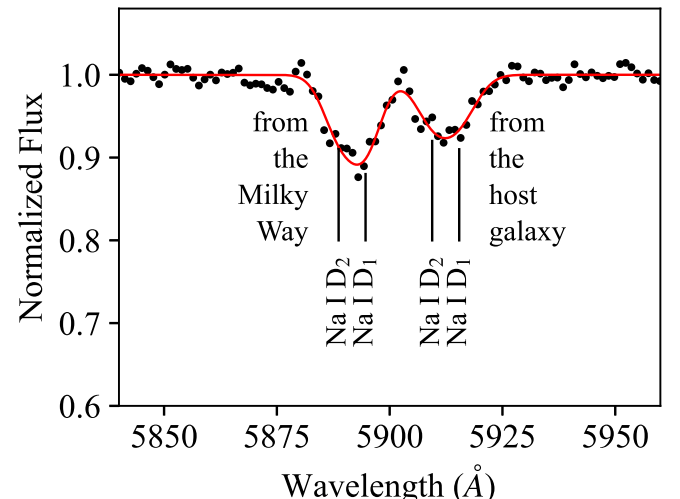


Fig. 2: Normalized Gemini spectrum of SN 2024abfl at $t = 3.2$ day, showing prominent Na I D absorption features. The observed data (black points) are fitted with Gaussian profiles (red curves). The left absorption component arises from the Milky Way, while the right one is associated with the host galaxy.

UV-band light curves decline sharply, which indicates a rapid cooling of the SN photosphere during the early phase. At the same time, the g - and B -band light curves show a slight decline,

whereas the *o*-, *r*-, *R*-, *i*-, and *I*-band light curves exhibit a slight rise.

The plateau has a typical magnitudes of $M_V \sim -15$ mag. During the plateau, the *r*-band magnitude of SN 2024abfl declines by less than 0.5 mag, and its *B*-band decline rate is 1.28 mag per 100 days, consistent with the characteristics of typical Type IIP supernovae (Li et al. 2011; Patat et al. 1994). We estimated the plateau length by fitting the analytic function provided in Valenti et al. (2016), as shown below:

$$y(t) = \frac{-a_0}{1 + e^{(t-t_{\text{PT}})/w_0}} + (p_0 \times t) + m_0 \quad (3)$$

where t is the time in days relative to the explosion; t_{PT} is the time in days from explosion to the transition point between the end of the plateau phase and start of the radioactive tail; a_0 represents the depth of the drop in magnitudes from the plateau to the radioactive tail; w_0 describes the slope of this drop; p_0 characterizes the slope on either side of the drop and m_0 is a constant. Setting the explosion time as $t = 0$, we fitted this function to the *V*-band light curve of SN 2024abfl, obtaining a best-fitting value of $t_{\text{PT}} = 126.54 \pm 0.65$ days. Figure 4 shows the *V*-band light curve of SN 2024abfl compared with other SNe IIP, showing that SN 2024abfl exhibits a relatively long plateau phase and low luminosity compared with most SNe IIP (Pastorello et al. 2004).

The plateau was followed by a sharp decline over the subsequent ~ 6 days, corresponding to a ~ 2 -magnitude drop in the *r* band from the plateau to the radioactive tail. All light curves decline slowly in the radioactive tail with a rate of ~ 0.9 mag per 100 days.

4.2. Bolometric Light Curve

We analyzed the evolution of the bolometric luminosity (L_{bol}), blackbody temperature (T_{BB}), and radius (R_{BB}) of SN 2024abfl using the SuperBol package (Nicholl 2018). Our analysis incorporated Swift UVOT (*uvw2*, *uvm2*, *uvw1*) and ground-based optical (*BVR*gri) photometry, with light curves in each band interpolated to the temporal sampling of the reference band and extrapolated where necessary assuming constant colors. As shown in Figure 5, the luminosity exhibits an initial peak of $\sim 3.8 \times 10^{41}$ erg s $^{-1}$, accompanied by a high temperature of $\sim 1.5 \times 10^4$ K and a small radius of $\sim 1.4 \times 10^{14}$ cm. As the shock-heated SN ejecta expands and cools, over the next ~ 10 days, the luminosity then decreases rapidly to $\sim 2.5 \times 10^{41}$ erg s $^{-1}$, the temperature also exhibits a rapid decline to ~ 7000 K, and the radius increases to $\sim 3.9 \times 10^{14}$ cm.

During the plateau phase, the sustained luminosity is primarily powered by radiative diffusion of the thermal energy released during the recombination of ionized hydrogen in the shock-heated envelope. Over this period, the temperature slightly decreases to ~ 5000 K, while the radius slightly expands to $\sim 5 \times 10^{14}$ cm.

After the plateau, the luminosity drops sharply to $\sim 3.3 \times 10^{40}$ erg s $^{-1}$ over a timescale of approximately 7 days, which marks the end of hydrogen recombination within the ejecta. Following this steep decline, SN 2024abfl enters the radioactive-decay tail, where the light curve is primarily powered by the energy deposited from the radioactive decay of ^{56}Co to ^{56}Fe . In this phase, the temperature remains roughly stable at ~ 3000 K, while the radius gradually decreases to $\sim 3 \times 10^{14}$ cm.

4.3. ^{56}Ni mass from the radioactive tail

^{56}Ni mass can be independently estimated from the tail L_{bol} by the following equation (Hamuy 2003), which back-traces the observed L_{bol} through the $^{56}\text{Ni} \rightarrow ^{56}\text{Co} \rightarrow ^{56}\text{Fe}$ decay chain to the amount of nickel originally synthesized:

$$M_{\text{Ni}} = 7.866 \times 10^{-44} \times L_{\text{t}} \exp \frac{(t - t_0)/(1 + z) - 6.1}{111.26} M_{\odot} \quad (4)$$

where z is the redshift, 6.1 is the half-life of ^{56}Ni in days, 111.26 is the e-folding time of the ^{56}Co decay in days, and t_0 is the explosion time. The tail luminosity of SN 2024abfl, $L_{\text{t}} = 1.5 \times 10^{40}$ erg s $^{-1}$, measured at ~ 235.73 days, implies a ^{56}Ni mass of $\sim 0.009 M_{\odot}$.

4.4. Analytical modelling

We also estimate the ^{56}Ni mass, the initial radius, the ejecta mass and the explosion energy of SN 2024abfl using the Markov Chain Monte Carlo (MCMC) version of the semi-analytic light curve code of Nagy et al. (2014) and Jäger et al. (2020). The model assumes homologously expanding, spherically symmetric ejecta of uniform density. Radiation transport is treated under the diffusion approximation, and the opacity is assumed to be piecewise constant, with $\kappa = 0.2 \text{ cm}^2 \text{ g}^{-1}$ in the ionized region and $\kappa = 0 \text{ cm}^2 \text{ g}^{-1}$ in the recombined, neutral region, separated by a recombination front propagating inward (Nagy & Vinkó 2016; Jäger et al. 2020). The luminosity is powered solely by the $^{56}\text{Ni} \rightarrow ^{56}\text{Co} \rightarrow ^{56}\text{Fe}$ radioactive decay chain, while contributions from circumstellar interaction or a binary companion are neglected. The γ -ray optical depth is parameterized as $\tau_{\gamma} = A_g/l^2$, where the parameter A_g controls the efficiency of energy deposition during the radioactive tail and, together with the nickel mass, determines the late-time luminosity.

We fit this model to the bolometric light curve of SN 2024abfl, exploring a parameter space defined by $R_0 \in (1-10) \times 10^{13}$ cm (the typical radius of RSGs), $M_{\text{ej}} \in 4-20 M_{\odot}$, $E_{\text{kin}} \in 0.001-1$ foe (1 foe = 10^{51} erg), $E_{\text{th}} \in 0.001-1$ foe, and $M_{\text{Ni}} \in 0.0005-0.25 M_{\odot}$ (see Table 3 for the explanations of these parameters). The resulting best-fitting parameters are listed in Table 3 and the best-fitting light curve is illustrated in Figure 6. The estimated ^{56}Ni mass is $\sim 0.009 M_{\odot}$, consistent with the value of $\sim 0.009 M_{\odot}$ derived from the tail bolometric luminosity. The ^{56}Ni mass, explosion energy, and ejecta mass are much lower than the typical range for normal SNe IIP (^{56}Ni mass: 0.001–0.26 M_{\odot} ; explosion energies: 0.1–5.5 foe; ejecta mass: 5.4–24.8 M_{\odot}) but consistent with LLSNe IIP (^{56}Ni mass: 0.001–0.025 M_{\odot} ; explosion energies: 0.1–0.28 foe) (Pastorello et al. 2004; Das et al. 2025a,b). It is noteworthy that our model does not fit the first peak, which as Gerard et al. (2026) suggested is caused by early-time circumstellar medium (CSM) interaction in SN 2024abfl.

5. Spectroscopic Analysis

The spectral sequence of SN 2024abfl is shown in Figure 7 and 8. From $t = 2.6$ to 4.6 days, the spectra exhibit a blue continuum as the primary component, with several broad P-Cygni profiles evident atop it. The most prominent are the $\text{H}\alpha$, $\text{H}\beta$, $\text{H}\gamma$ and $\text{He I } \lambda 5876$ lines. As the ejecta expands and cools, the continuum becomes increasingly red out to $t = 31.4$ days. From $t = 31.4$ to 119.3 days (during the plateau phase), the $\text{H}\alpha$ emission component becomes increasingly prominent and metal lines begin to

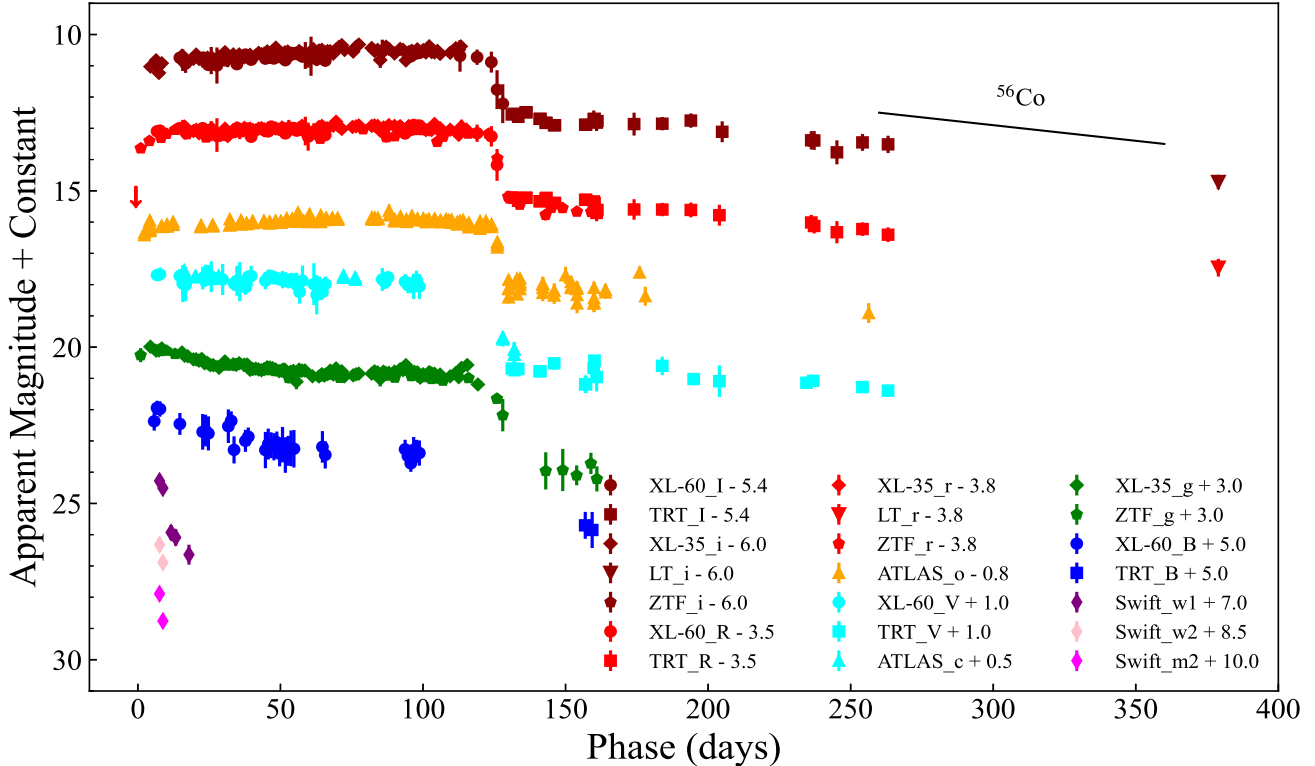


Fig. 3: The multi-band light curves of SN 2024abfl. The phase represents days relative to the date of explosion, $t_0 = 60627.27$ MJD.

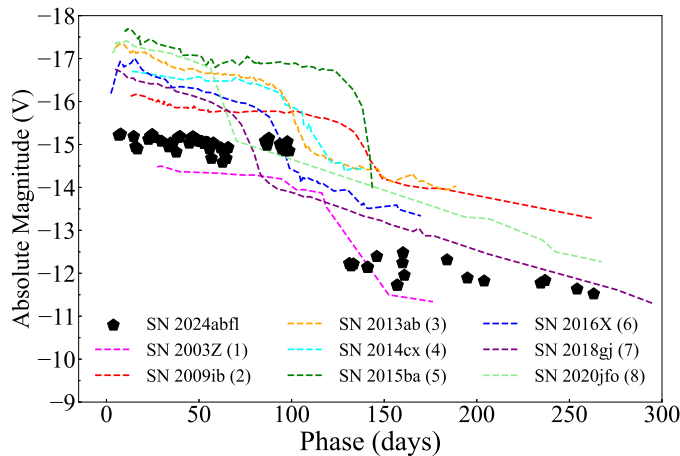


Fig. 4: The V-band light curve of SN 2024abfl compared with other SNe IIP. (1) Spiro et al. (2014), (2) Takáts et al. (2015), (3) Bose et al. (2015), (4) Huang et al. (2016), (5) Dastidar et al. (2018), (6) Huang et al. (2018), (7) Teja et al. (2023), (8) Teja et al. (2022).

emerge, such as Fe II ($\lambda\lambda 5169, 5018, 4924$) and Ca II infrared (IR) triplet ($\lambda\lambda 8498, 8542, 8662$). During the nebular phase, the decay of ^{56}Ni becomes the primary power source. As the ejecta become optically thin, the absorption components of the P-Cygni profiles disappear. The spectra at $t = 140.3$ days and onwards, shown in Figure 8, are dominated by H α , Na I D, and the Ca II IR triplet emission, with the H α line remaining the most prominent feature.

Table 3: The best-fitting parameters for bolometric light curve of SN 2024abfl using Nagy et al. (2014) and Jäger et al. (2020).

Parameter	Best-fitting value	Remarks
R_0 (10^{13}cm)	$6.8^{+1.8}_{-5.6}$	Initial radius of ejecta
M_{ej} (M_{\odot})	$8.3^{+5.9}_{-2.8}$	Ejecta mass
M_{Ni} (M_{\odot})	$0.009^{+0.089}_{-0.009}$	Initial ^{56}Ni mass
E_{kin} (foe)	$0.42^{+0.18}_{-0.41}$	Initial kinetic energy
E_{th} (foe)	$0.03^{+0.11}_{-0.03}$	Initial thermal energy

5.1. Kinematics

Figure 9 shows the evolution of H α line profile from $t = 2.6$ to 119.3 days (during the plateau phase). The data show a decline in expansion velocity due to the recession of the photosphere in the SN ejecta with lower velocities in the interior. The velocity of H α absorption dip decreased from $\sim 3800 \text{ km s}^{-1}$ at $t = 31.4$ days to $\sim 3400 \text{ km s}^{-1}$ at $t = 34.5$ days, and further declined to $\sim 2800 \text{ km s}^{-1}$ at $t = 39.6$ days. These velocities are much lower than normal SNe IIP at similar epochs ($> 4500 \text{ km s}^{-1}$ at < 50 days; Hamuy 2003). From $t = 39.6$ days, a high-velocity absorption feature emerges at -4200 km s^{-1} . This is possibly due to a plume of matter in the inner ejecta moving toward us at a higher velocity. In addition, two emission features show up at $\pm 2000 \text{ km s}^{-1}$ from $t = 63.5$ days. It is possible that the SN ejecta is colliding with two clumps of CSM, which were ejected by the

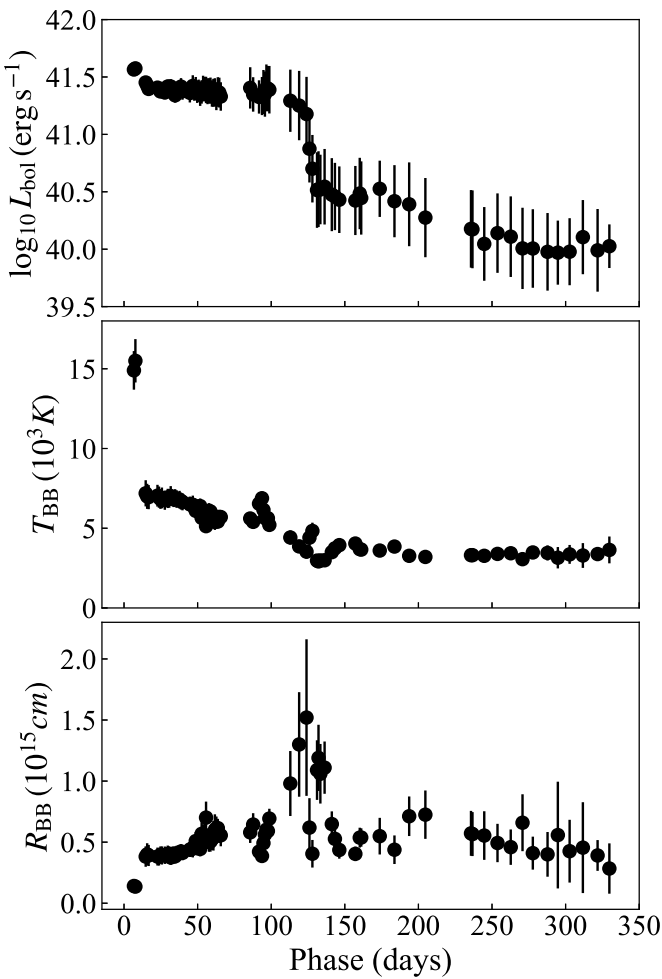


Fig. 5: *Top panel*: Logarithmic bolometric luminosity (L_{bol}) from observed fluxes. *Middle panel*: Evolution of the blackbody temperature (T_{BB}). *Bottom panel*: Evolution of the blackbody radius (R_{BB}). All parameters are shown as a function of days since explosion (MJD 60627.27).

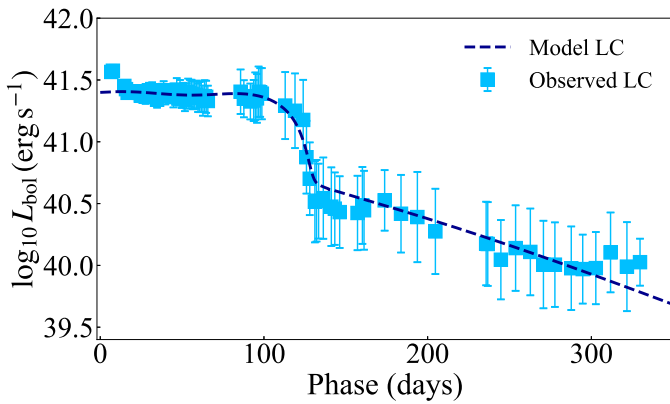


Fig. 6: The best-fitting analytical model light curve of SN 2024abfl using [Nagy et al. \(2014\)](#) and [Jäger et al. \(2020\)](#). The phase represents days relative to the date of explosion, $t_0 = 60627.27$ MJD.

progenitor before its explosion. [Gerard et al. \(2026\)](#) also found these features and explained it as the interaction with CSM.

5.2. Nebular phase

At the nebular phase, the $[\text{O I}] \lambda\lambda 6300, 6364$ lines primarily originate from the cooling radiation of the oxygen-rich zone; their intensity is directly related to the oxygen mass, serving as an important tracer for inferring the progenitor star mass. Meanwhile, the $[\text{Ca II}] \lambda\lambda 7291, 7323$ lines mainly arise from the primordial calcium (solar abundance) in the hydrogen envelope of the progenitor, reprocessing deposited energy; their intensity reflects the mass of the hydrogen-rich region and the degree of ^{56}Ni mixing ([Alsabti & Murdin 2017](#)). The flux ratio $[\text{O I}]/[\text{Ca II}]$ reflects the mass distribution structure between the stellar core and the envelope, which is determined by the initial mass of the star. Therefore, measuring this flux ratio in nebular phase spectra allows for the estimation of the progenitor star's mass.

In our observations, the forbidden calcium emission lines $[\text{Ca II}] \lambda\lambda 7291, 7324$ are clearly visible, whereas the $[\text{O I}] \lambda\lambda 6300, 6364$ lines remain buried in the noise. We measured the flux of the $[\text{Ca II}]$ line and estimated the upper limit of $[\text{O I}]$ line flux. We fitted the $[\text{Ca II}]$ feature with a Gaussian profile, assumed that the $[\text{O I}]$ lines share the same width, and adopted 3 times the continuum noise near $[\text{O I}]$ as the upper limit of the line height. At $t = 196.3$ days, the flux ratio $[\text{O I}]/[\text{Ca II}]$ is smaller than 0.75. By comparing with the flux ratios obtained from the modeled spectra with different progenitor masses at a similar epoch ([Jerkstrand et al. 2012, 2014](#); [Ferrari et al. 2024](#)), we estimate the progenitor mass to be $\leq 15 M_{\odot}$. This is consistent with the result of [Luo et al. \(2025\)](#) based on the detection of the progenitor and [Gerard et al. \(2026\)](#) derived from the nebular spectra ($9-12 M_{\odot}$).

6. Summary and Discussion

We present photometric and spectroscopic observations and analysis of SN 2024abfl, a SN IIP in the nearby galaxy NGC 2146. It has a relatively long plateau phase of ~ 126.5 days, suggesting a thick hydrogen envelope. The absolute magnitude of the plateau is $M_V \sim -15$ mag, which is much lower than those of normal SNe IIP. By fitting a semi-analytical model to the bolometric light curves, we estimated a ^{56}Ni mass of $\sim 0.009 M_{\odot}$, an initial kinetic energy of ~ 0.42 foe, an initial thermal energy of ~ 0.03 foe, a progenitor radius of $\sim 6.8 \times 10^{13}$ cm and an ejecta mass of $\sim 8.3 M_{\odot}$. The ^{56}Ni mass is consistent with the value derived independently from the tail bolometric luminosity.

The spectra of SN 2024abfl are characterized by an early blue continuum that turns red over time, several broad P-Cygni features from $\text{H}\alpha$, Ca II , Fe II and Na I D during the photospheric phase and low velocity ($\sim 3800 \text{ km s}^{-1}$ at $t = 31.4$ days). From $t = 37.3$ days, a high-velocity $\text{H}\alpha$ absorption feature emerges, possibly due to a plume of matter in the inner ejecta moving toward us at a higher velocity. From $t = 61.2$ days, two emission features show up at $\pm 2000 \text{ km s}^{-1}$, possibly caused by CSM interaction. The SN enters the nebular phase from $t = 138.0$ days and we estimate the progenitor mass to be $\leq 15 M_{\odot}$ by the flux ratio of $[\text{O I}]/[\text{Ca II}]$. This is consistent with the progenitor mass inferred from the direct detection.

[Gerard et al. \(2026\)](#) reported a slightly fainter peak absolute magnitude of SN 2024abfl in the V band as -14.9 mag, which is likely due to their adoption of a lower extinction value ($E(B-V)_{\text{tot}} = 0.28 \pm 0.11$) compared to our estimates. The low values for the ^{56}Ni mass, ejecta mass, and explosion energy estimated by [Gerard et al. \(2026\)](#) and [Das et al. \(2025b\)](#) are consistent with our values within uncertainties, supporting the classification of SN 2024abfl as a LLSN.

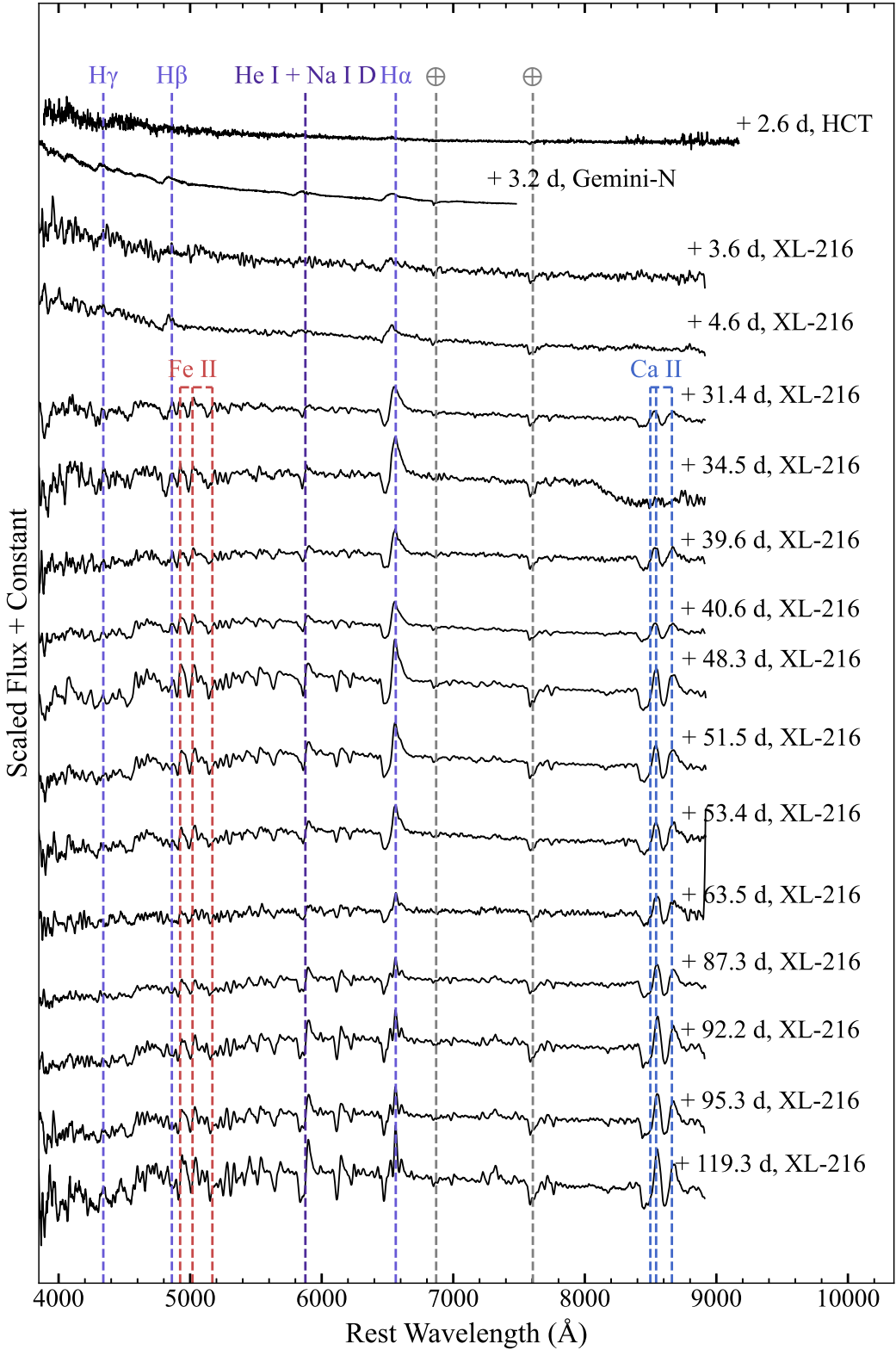


Fig. 7: Spectroscopic evolution of SN 2024abfl. The displayed spectra have not been corrected for interstellar reddening. The redshift of the host galaxy ($z = 0.002979$, as reported by TNS) has been corrected. The phase represents days relative to the date of explosion, $t_0 = 60627.27$ MJD.

Compared with the typical range for SNe IIP (^{56}Ni mass: 0.001–0.26 M_\odot ; explosion energy: 0.1–5.5 foe; ejecta mass: 5.4–24.8 M_\odot), SN 2024abfl has a lower ^{56}Ni mass, lower explosion energy, and lower ejecta mass. These parameters fall within the

range of LLSNe IIP (^{56}Ni mass: 0.001–0.025 M_\odot ; explosion energy: 0.1–0.28 foe; progenitor mass: 8–12 M_\odot) (Pastorello et al. 2004; Das et al. 2025a,b). The low progenitor mass (9–12 M_\odot ; Luo et al. 2025; Gerard et al. 2026) once again provides evi-

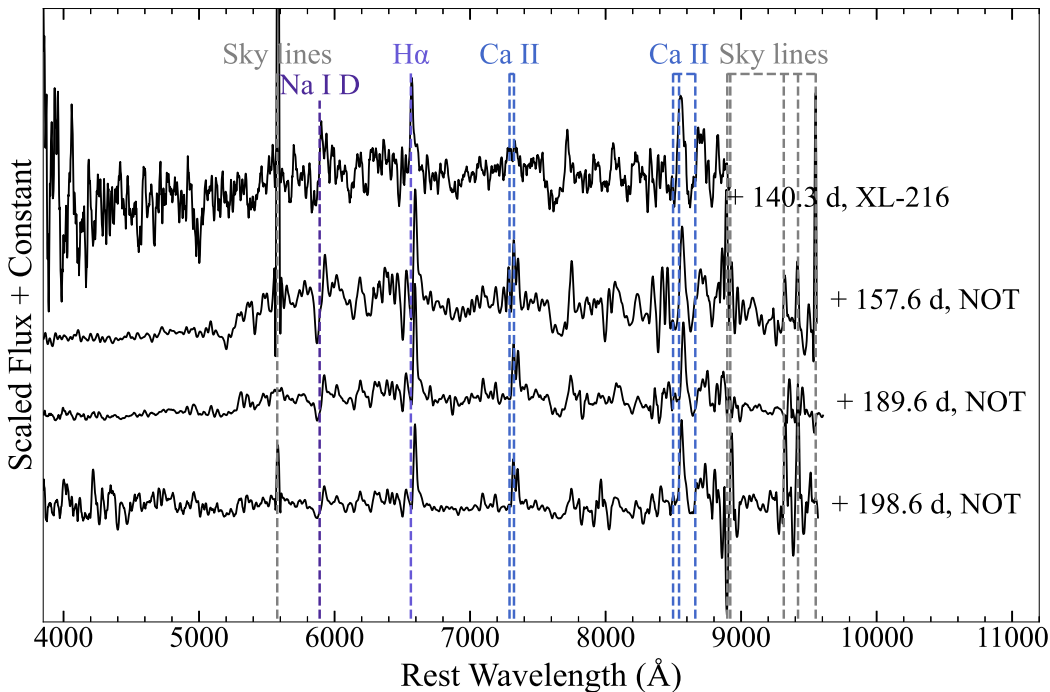


Fig. 8: Same as Figure 7 but for later epochs.

dence that LLSNe IIP originate from low-mass RSG progenitor stars.

Acknowledgements

ZF is supported by the Strategic Priority Research Program of the Chinese Academy of Sciences, Grant No. XDB0550100. NCS is funded by the Strategic Priority Research Program of the Chinese Academy of Sciences Grant No. XDB0550300, the National Natural Science Foundation of China Grants No.12303051 and No.12261141690, and the China Manned Space Program No. CMS-CSST-2025-A14. We acknowledge the support by the National Astronomical Research Institute of Thailand under the project number TRTC11A_004, TRTToO_2024002, TRTToO_2024004, TRTToO_2024005, TRTToO_2024006, TRTC12A_003, TRTC12B_003 and TRTC12C_003. JL is supported by the National Natural Science Foundation of China (NSFC; grant No. 12273027). ZG is supported by the China-Chile Joint Research Fund (CCJRF No.2301) and the Chinese Academy of Sciences South America Center for Astronomy (CASSACA) Key Research Project E52H540301. This work was supported by the National Research and Development Agency (ANID) through the FONDECYT Iniciación project Grant No. 11260176. FP acknowledges support from the MICINN under grant numbers PID2022-141915NB-C21. ZXN is funded by the NSFC Grant No. 12303039.

We thank the staff at all participating observatories, including the Xinglong-35cm, 60-cm and 2.16-m telescopes, the Liverpool Telescope, the Thai Robotic Telescope network, and the Nordic Optical Telescope, for their support during our observing campaigns.

We acknowledge the use of data and services provided by ATLAS, ZTF, Swift/UVOT and the Transient Name Server (TNS). This research has made use of NASA's Astrophysics Data System (ADS). The ZTF forced-photometry service was

funded under the Heising-Simons Foundation grant #12540303 (PI: Graham). We also acknowledge the use of open-source software packages including ASTROPY, AUTOPHOT, and IRAF. We also acknowledge the use of open-source software packages including astropy (Astropy Collaboration et al. 2018, 2022), AutoPhot (Brennan & Fraser 2022), IRAF (Tody 1986) and SuperBol (Nicholl 2018).

Facilities: LT, NOT, TRT, XL-35, XL-60, XL-216

Software: astropy (Astropy Collaboration et al. 2018, 2022), AutoPhot (Brennan & Fraser 2022), IRAF (Tody 1986), SuperBol (Nicholl 2018)

References

Adamo, A., Gallagher, J. S., Smith, L., et al. 2012a, in American Astronomical Society Meeting Abstracts, Vol. 219, American Astronomical Society Meeting Abstracts #219, 438.03

Adamo, A., Smith, L. J., Gallagher, J. S., et al. 2012b, MNRAS, 426, 1185

Alsabti, A. W. & Murdin, P. 2017, Handbook of Supernovae

Andrews, J., Bostroem, K. A., Sand, D. J., et al. 2024, Transient Name Server Classification Report, 2024-4535, 1

Arcavi, I. 2017, in Handbook of Supernovae, ed. A. W. Alsabti & P. Murdin, 239

Arnett, W. D. 1980, ApJ, 237, 541

Astropy Collaboration, Price-Whelan, A. M., Lim, P. L., et al. 2022, ApJ, 935, 167

Astropy Collaboration, Price-Whelan, A. M., Sipőcz, B. M., et al. 2018, AJ, 156, 123

Bose, S., Valenti, S., Misra, K., et al. 2015, MNRAS, 450, 2373

Bottinelli, L., Gouguenheim, L., Paturel, G., & de Vaucouleurs, G. 1983, A&A, 118, 4

Brennan, S. J. & Fraser, M. 2022, A&A, 667, A62

Callis, E., Fraser, M., Pastorello, A., et al. 2021, How low can you go? SN 2018zd as a low-mass Fe core-collapse supernova

Cardelli, J. A., Clayton, G. C., & Mathis, J. S. 1989, ApJ, 345, 245

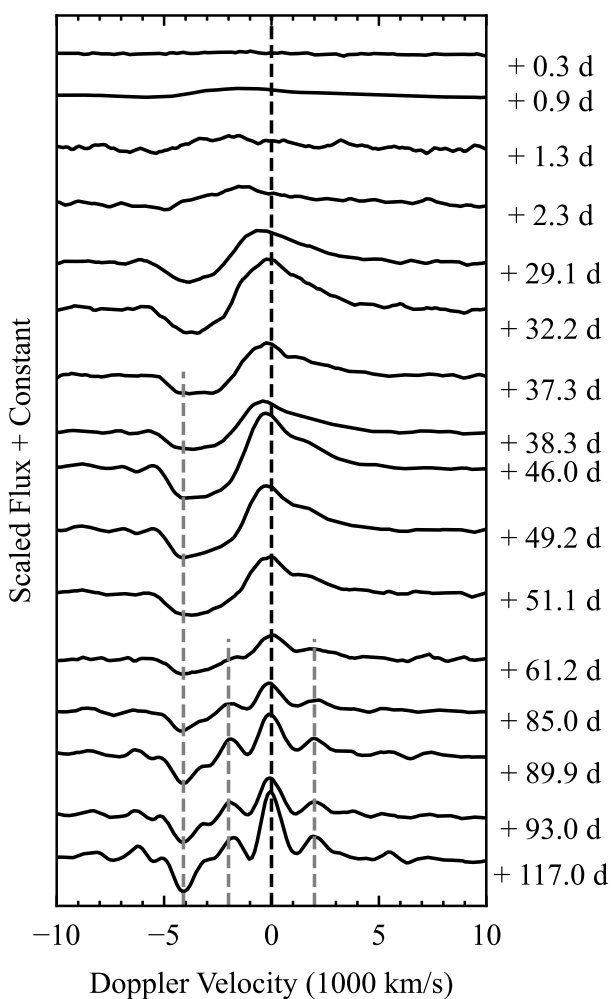
Chevalier, R. A. 1976, ApJ, 207, 872

Das, H., Sahu, D. K., Singh, A., Kawabata, K., & Teja, R. 2024, Transient Name Server Classification Report, 2024-4515, 1

Das, K. K., Kasliwal, M. M., Fremling, C., et al. 2025a, PASP, 137, 044203

Das, K. K., Kasliwal, M. M., Sollerman, J., et al. 2025b, arXiv e-prints, arXiv:2506.20068

Dastidar, R., Misra, K., Hosseinzadeh, G., et al. 2018, MNRAS, 479, 2421



Lovegrove, E. & Woosley, S. E. 2013, *ApJ*, 769, 109
 Luo, J., Zhang, L., Chen, B.-Q., et al. 2025, *ApJ*, 982, L55
 Masci, F. J., Laher, R. R., Rusholme, B., et al. 2018, *PASP*, 131, 018003
 Nadezhin, D. K. 1980, *Ap&SS*, 69, 115
 Nagy, A. P., Ordasi, A., Vinkó, J., & Wheeler, J. C. 2014, *A&A*, 571, A77
 Nagy, A. P. & Vinkó, J. 2016, *A&A*, 589, A53
 Nicholl, M. 2018, *Research Notes of the American Astronomical Society*, 2, 230
 Niu, Z., Sun, N.-C., Maund, J. R., et al. 2023, *ApJ*, 955, L15
 Olivares E., F., Hamuy, M., Pignata, G., et al. 2010, *ApJ*, 715, 833
 Pastorello, A., Zampieri, L., Turatto, M., et al. 2004, *Monthly Notices of the Royal Astronomical Society*, 347, 74
 Patat, F., Barbini, R., Cappellaro, E., & Turatto, M. 1994, *A&A*, 282, 731
 Poznanski, D., Prochaska, J. X., & Bloom, J. S. 2012, *MNRAS*, 426, 1465
 Schlafly, E. F. & Finkbeiner, D. P. 2011, *ApJ*, 737, 103
 Smartt, S. J. 2009, *ARA&A*, 47, 63
 Spiro, S., Pastorello, A., Pumo, M. L., et al. 2014, *MNRAS*, 439, 2873
 Suzuki, A. & Shigeyama, T. 2025, *MNRAS*, 543, 3929
 Takáts, K., Pignata, G., Pumo, M. L., et al. 2015, *MNRAS*, 450, 3137
 Teja, R. S., Singh, A., Sahu, D. K., et al. 2023, *ApJ*, 954, 155
 Teja, R. S., Singh, A., Sahu, D. K., et al. 2022, *ApJ*, 930, 34
 Terry, J. N., Paturel, G., & Ekholm, T. 2002, *A&A*, 393, 57
 Tody, D. 1986, in *Society of Photo-Optical Instrumentation Engineers (SPIE) Conference Series*, Vol. 627, *Instrumentation in astronomy VI*, ed. D. L. Crawford, 733
 Tonry, J. L., Denneau, L., Heinze, A. N., et al. 2018, *PASP*, 130, 064505
 Valenti, S., Howell, D. A., Stritzinger, M. D., et al. 2016, *MNRAS*, 459, 3939
 Van Dyk, S. D., Li, W., & Filippenko, A. V. 2003, *PASP*, 115, 1289
 Zhao, Y.-H., Hong, X., Sun, N.-C., et al. 2025, *ApJ*, 992, L24

Fig. 9: Evolution of H α line profiles during the photospheric phase.

Davies, B. & Beasor, E. R. 2018, *MNRAS*, 474, 2116
 de Jager, C. 1998, *A&A Rev.*, 8, 145
 De Vis, P., Jones, A., Viaene, S., et al. 2019, *A&A*, 623, A5
 Ekström, S., Georgy, C., Eggenberger, P., et al. 2012, *A&A*, 537, A146
 Eldridge, J. J. & Tout, C. A. 2004, *MNRAS*, 353, 87
 Falk, S. W. & Arnett, W. D. 1977, *ApJS*, 33, 515
 Ferrari, L., Folatelli, G., Ertini, K., Kuncarayakti, H., & Andrews, J. E. 2024, *A&A*, 687, L20
 Filippenko, A. V. 1997, *ARA&A*, 35, 309
 Fraser, M. 2016, *MNRAS*, 456, L16
 Georgy, C. 2012, *A&A*, 538, L8
 Gerard, M., Andrews, J. E., Clayton, G. C., et al. 2026, *arXiv e-prints*, arXiv:2601.02638
 Grassberg, E. K., Imshennik, V. S., & Nadyozhin, D. K. 1971, *Ap&SS*, 10, 28
 Hamuy, M. 2003, *ApJ*, 582, 905
 Heger, A., Fryer, C. L., Woosley, S. E., Langer, N., & Hartmann, D. H. 2003, *ApJ*, 591, 288
 Hiramatsu, D., Howell, D. A., Van Dyk, S. D., et al. 2021, *Nature Astronomy*, 5, 903
 Hong, X., Sun, N.-C., Niu, Z., et al. 2024, *ApJ*, 977, L50
 Huang, F., Wang, X., Zampieri, L., et al. 2016, *ApJ*, 832, 139
 Huang, F., Wang, X.-F., Hosseinzadeh, G., et al. 2018, *MNRAS*, 475, 3959
 Itagaki, K. 2024, *Transient Name Server Discovery Report*, 2024-4506, 1
 Jäger, Jr., Z., Vinkó, J., Bíró, B. I., et al. 2020, *MNRAS*, 496, 3725
 Jerkstrand, A., Fransson, C., Maguire, K., et al. 2012, *A&A*, 546, A28
 Jerkstrand, A., Smartt, S. J., Fraser, M., et al. 2014, *MNRAS*, 439, 3694
 Kochanek, C. S. 2014, *ApJ*, 785, 28
 Li, W., Leaman, J., Chornock, R., et al. 2011, *MNRAS*, 412, 1441